https://doi.org/10.26599/JAC.2023.9220717

Research Article

Oxygen vacancy-rich MoO_3 nanorods as photocatalysts for photo-assisted Li–O_2 batteries

Guiru Sun, Daming Yang, Zexu Zhang, Yan Wang, Wei Lu, Ming Feng*

Key Laboratory of Functional Materials Physics and Chemistry of the Ministry of Education, Jilin Normal University, Changchun 130103, China

* Corresponding author.

E-mail: mingfeng@jlnu.edu.cn

Received: October 26, 2022; Revised: December 16, 2022; Accepted: January 4, 2023

Abstract: Photo-assisted Li-O_2 batteries have been developed as a new system to reduce the large overpotential in Li-O_2 batteries. However, the constructing an optimized photocatalyst is still a challenge to achieve the broad light absorption and low recombined rate of photoexcited electrons and holes. Herein, the oxygen vacancy-rich MoO_3 (MoO_{3-x}) nanorods are employed as photocatalyst to accelerate the kinetics of cathode reactions in photo-assisted Li-O_2 batteries. The oxygen vacancy on MoO_{3-x} nanorods can not only increase light harvesting capability but also improve the electrochemical activity for cathode reactions. Under illumination, the photoexcited electrons and holes are effectively

separated on MoO_{3-x} nanorods. During discharging, the activate O_2 is reduced to Li_2O_2 by photoexcited electrons from MoO_{3-x} nanorods. The photoexcited holes can promote the decomposition of Li_2O_2 during subsequent charging. According, the photo-assisted Li-O_2 batteries with MoO_{3-x} nanorods deliver an ultralow overpotential of 0.22 V, a considerable rate capability, and a good reversibility. We think that this work could give a reference for the exploitation and application of photocatalysts in photo-assisted Li-O_2 batteries.

Keywords: MoO_3 nanorods; oxygen vacancy; photocatalyst; photo-assistance; Li-O_2 batteries

1 Introduction

The lithium-oxygen (Li-O_2) battery is a promising energy storage system due to its high theoretical energy density (~3500 Wh kg^{-1}), which is operated with Li_2O_2-redox reaction ($2Li^+ + O_2 + 2e^- \leftrightarrow Li_2O_2$, $E^0 = 2.96$ V) [1-3]. Unfortunately, Li-O_2 batteries face many tough problems, among which the sluggish kinetics of the cathode lead to a large overpotential, low round-trip efficiency, and limited cycle of Li-O_2 batteries [4-6]. It is reported that the sluggish kinetics are associated with the passivated cathode surface by Li_2O_2. The generated Li_2O_2 will obstruct the charge transfer and hinders the O_2 diffusion on cathode because it is a wide band gap insulator and does not dissolve in the electrolyte [7-9]. To improve the reaction kinetics, some electrocatalysts (*e.g.*, noble and transition metal-based materials) were introduced in cathode [9-12]. Unfortunately, the rare and expensive noble metals and the limited catalytic activity of transition metals hinder their widely practical application. Thus, it is expected to seek cut-price and flexible means for accelerating the reaction kinetics of Li-O_2 batteries.

Recently, the employment of light has been proved that can promote the generation and oxidation of Li_2O_2, especially reduce the overpotential in photo-assisted Li-O_2 batteries [13-16]. Under light irradiation, a semiconductor-containing cathode contributes to separating the electrons and holes in conduction bands (CB) and valence bands (VB), respectively [15-18]. In an ideal system, the photoelectrons are able to boost the formation of Li_2O_2 during oxygen reduction reaction (ORR), while

the holes could facilitate the decomposition of Li_2O_2 during oxygen evolution reaction (OER) [19]. Thus, the semiconductor catalyst is regarded as the key that affects the performance of photo-assisted Li-O_2 batteries [20]. Among the family semiconductor materials, orthorhombic molybdenum trioxide (α-MoO_3) as the photocatalyst plays a major role in the field of photocatalysis because of its nontoxicity, low-price, and good chemical stability [21,22]. The various morphologies and structures of MoO_3 were developed to improve their photocatalytic activity, such as nanobelts [23], nanorods [24], and nanotubes [25]. Unfortunately, these MoO_3 species show low photocatalytic ability in practical application under visible light, which could result from two reasons: (i) MoO_3 as n-type semiconductor with a wide band gap (3.2 eV) has a low utilization rate for visible light [26]; (ii) the photo-excited electrons and holes easily recombine [27]. Therefore, it is highly desirable to broad the range of light absorption and improve the separation efficiency of electron and hole for enhancing the photocatalytic activity of MoO_3.

To address the mentioned challenges, the research focused on construction of defects engineering (usually oxygen defects) to improve photocatalytic performance of semiconductor materials by tuning their electronic structure and surface properties [28]. Very recently, we demonstrated that titanium dioxide (TiO_2) as photocatalysts show superior catalytic ability in photo-assistance Li-O_2 batteries though introducing of oxygen vacancies [14]. It is expected to obtain a similar effect for MoO_3 with oxygen vacancies (*i.e.*, MoO_{3-x}). More importantly, it has been proved that the oxygen vacancies in MoO_3 interact strongly with active oxygen from the battery environment (*e.g.,* O_2, LiO_2, and Li_2O_2), which plays a key role during the discharge and charge processes of Li-O_2 batteries [29]. Although the photocatalytic behavior of MoO_{3-x} has been reported by previously works, its catalytic mechanism in photo-assisted Li-O_2 batteries has rarely been mentioned. Therefore, it is significant the employment of MoO_{3-x} as photocatalyst and understanding its catalytic mechanism in photo-assisted Li-O_2 batteries.

In this study, the MoO_{3-x} nanorods were fabricated by combining solvothermal and hydrogen-thermal reduction methods, which were used as photocatalysts in photo-assisted Li-O_2 batteries. By

introducing oxygen vacancies, the light response and photocatalytic ability of MoO_{3-x} nanorods are significantly increased. The photoexcited electrons and holes on the MoO_{3-x} nanorods were separated effectively with light irradiation. The photoexcited electrons are beneficial to the O_2 reduction to form Li_2O_2 during discharge. The generated Li_2O_2 is decomposed to O_2 and Li^+ ion by the holes during charging. The photo-assisted Li-O_2 batteries with MoO_{3-x} nanorods showed an ultralow overpotential of 0.22 V, a good rate performance, and a superior reversibility. This work could offer an opportunity for the design of high active photocatalysts in photo-assisted Li-O_2 batteries.

2 Experimental

2. 1 Chemicals and materials

All reagents and solvents were commercially available. Hydrogen peroxide (H_2O_2, AR, Sinopharm Chemical Reagent Co., Ltd. 30%), nitric acid (HNO_3, AR, Sinopharm Chemical Reagent Co., Ltd.), molybdenum trioxide (MoO_3, AR, Aladdin Reagent), and Li foil (China Energy Lithium Co., Ltd.). Tetraethylene glycol dimethyl ether (TEGDME, AR, Aladdin Reagent, 99.7%) and N-methyl-pyrrolidone (NMP, AR, Aladdin Reagent, 99%) were dried with activated molecular sieves (Type 4 Å, Sinopharm Chemical Reagent Co., Ltd.) for 7 days. Carbon paper (CP, CeTech Co., Ltd.), super P (SP, Timcal, ~50 nm), polyvinylidene fluoride (PVDF, DuPont Company, 99.9%), lithium bis(trifluoromethane sulfonimide) (LiTFSI, AR, Aladdin Reagent), and glass fiber separator (GF/D, Whatman) are dried under a vacuum oven (120 ˚C, 24 h).

2. 2 Preparation of MoO_{3-x} nanorods

MoO_3 (3.6 g) was added into H_2O_2 (27 mL) to form a solution with vigorous stirring. HNO_3 (13.5 mL) and distilled water (65 mL) were then mixed with above solution. After stirring for 30 min, the obtained mixture was transferred to Teflon-lined autoclave (50 mL) and heated at 170 °C for 24 h. The precipitate was separated by centrifugation, washing, and drying (50 ˚C for 24 h), which is MoO_3

nanorods. The MoO_{3-x} nanorods were synthesized by hydrogen-thermal reduction the MoO_3 nanorods at 350 °C for 2 h with H_2 and Ar mixture gas flow (8:92).

2. 3 Characterizations

X-ray Diffraction (XRD, D/ MAX-2500 /PC, Rigaku) was employed to gather the XRD patterns of the all the samples. The Raman spectra of the products were acquired using the Micro Raman system (LabRAM HR spectrometer, Horiba) with an Ar ion laser (514 nm) and an Olympus BX microscope. The X-ray photoelectron spectroscopy (XPS, ESCALAB 250XI, Thermo Fisher Scientific) was used to examine the valence state of elements. The microstructure and morphology of all samples were identified by scanning electron microscope (SEM, S-5500, Hitachi) and transmission electron microscope (TEM, Talos F200X G2, Thermo Fisher Scientific) with energy dispersive X-ray (EDX) and high-angle annular darkfield scanning TEM (HAADF-STEM). the photoluminescence (PL) spectra of as-prepared samples were recorded on a spectrofluorometer (F-4600, Hitachi) at 25 ˚C in ambient air. The ultraviolet visible spectrophotometer (UV-vis, UV-3600, Shimadzu) were performed to collect UV-vis absorption spectra of as-prepared products. Electron spin resonance (ESR, JES-FA200, JELO) was utilized to monitor the unpaired electrons in as-prepared samples.

2. 4 Assembly of Li-O_2 cells

In order to obtain the slurry, the SP, MoO_{3-x} nanorods, and PVDF were added to NMP at weight ratios of 6: 3: 1. The cathodes were prepared by coating the slurry on CP with diameter of 13 mm and thickness of ~20 μm, which were then dried in vacuum at 70˚C for 12 h for removing the excess solvent. The mass loadings of SP and MoO_{3-x} nanorods in the cathode are 0.2 and 0.1 mg, respectively. The coin-type cells (CR2025) were assembled using the Li foil anode, the GF separator soaked in an electrolyte (135 μL, 1 M LiTFSI/TEGDME), and the cathode within an argon-filled glovebox (SG2400/750TS, Vigor, H_2O and O_2 < 1 ppm). For transmission of light and O_2, the cathode shells were punched to form a hole with a diameter of 10 mm.

2. 5 Electrochemical measurements

The obtained cells were tested in an O_2-filled glovebox (SG2400/750TS, Vigor, H_2O and O_2 < 1 ppm) at various current densities of 100-500 mA g^{-1} under various fixed capacities of 500-1000 mAh g^{-1} on the system (CT-ZWJ-4'S-010, NEWARE). Note that the current density and specific capacity were calculated based on the mass of SP. For testing photo-assisted Li-O_2 cells, a gelS500/350 Xe-lamp was employed as light source. The light intensity for the cathode surface was locked. The testing platform of photo-assisted Li-O_2 cells was shown in Fig. S1 in Electronic Supplementary Material (ESM). Cyclic voltammetry (CV) curves were recorded at a scan rate of 0.1 mV s^{-1} with a voltage ranging of 2.2-4.5 V vs. Li/Li^+. Linear sweep voltammetry (LSV) curves were obtained at a scan rate of 0.5 mV s^{-1}. Electrochemical impedance spectroscopy (EIS) was gathered with the frequency range (10^{-2}-10^5 Hz) and an amplitude of 0.005 V. The CV, LSV, and EIS were performed on an electrochemical workstation (Solartron 1470E, AMETEK) at room temperature. A customized Swagelok type of Li-O_2 cell with a quartz window and two PEEK capillary tubes were designed for the differential electrochemical mass spectrometry (DEMS) on a commercial quadrupole mass spectrometer (Hiden HPR-20).

3 Results and discussion

The crystal structure of MoO_3 and MoO_{3-x} nanorods were evaluated, as shown in Fig. 1A. The XRD peaks could be assigned to the standard pattern of orthorhombic phase α-MoO_3 (JCPDS No. 05–0508) [26]. The main XRD peaks are consistent with the crystal planes of (020), (040), and (060), respectively, demonstrating the highly preferred orientations. Compared with the pristine MoO_3 nanorods, the peak corresponding to the (040) crystal plane for MoO_{3-x} nanorods shifts to high angle (Fig. 1B), which arises from the expansion of interlamellar spacing owe to the presence of oxygen vacancies [27]. In Fig. 1C, a set of typical Raman peaks were observed for MoO_3 and MoO_{3-x} nanorods, which is consistent with the previously work [28]. The peaks at 280, 373, and 990 cm^{-1} are ascribed to the wagging vibration, bending vibration, and stretching vibration of the terminal oxygen (Mo=O),

150 respectively [30, 31]. The peaks at 334 and 660 cm^{-1} represent the bending vibration and stretching
151 vibration of triple coordinated oxygen (Mo_3−O), respectively [32], and that at 818 cm^{-1} could be
152 caused by the double coordinated oxygen (Mo_2−O) stretching vibration [33]. Note that a slight blue
153 shift of the peak at 818 cm^{-1} for MoO_{3-x} nanorods compared to that of the pristine MoO_3 nanorods
154 was observed (Fig. 1D), resulting from the phonon confinement by point defects [27,28].

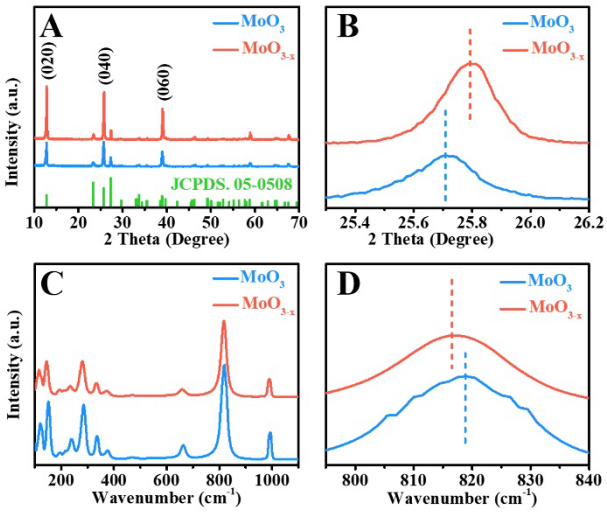

155

156 **Fig. 1** (A) XRD patterns and (B) corresponding magnified pattern of MoO_3 and MoO_{3-x} nanorods, (C)
157 Raman spectra and (D) corresponding magnified pattern of MoO_3 and MoO_{3-x} nanorods.

158

159 The element compositions and states of MoO_3 and MoO_{3-x} nanorods were evaluated by using XPS.
160 The survey spectra for both samples are displayed in Fig. 2A, which shows the presence of Mo and O
161 without any other elements. The atomic ratios are 1:3.33 and 1:2.84 for Mo and O in MoO_3 and MoO_{3-x},
162 respectively, confirming that oxygen vacancies are successfully generated in MoO_{3-x} nanorods. In Fig.
163 2B, the Mo 3d spectrum is deconvoluted into one pair of peaks at 232.9 and 236.0 eV for MoO_3
164 nanorods, corresponding to the Mo $3d_{5/2}$ and Mo $3d_{3/2}$ of Mo^{6+}, respectively [34]. In contrast, the Mo
165 3d spectrum for MoO_{3-x} nanorods exhibits a new pair of peaks at 231.5 and 234.6 eV (Fig. 2C) that
166 represent the Mo $3d_{5/2}$ and Mo $3d_{3/2}$ of Mo^{5+}, respectively [35], implying the existence of oxygen
167 vacancies in MoO_{3-x} nanorods. The O 1s spectra for MoO_3 and MoO_{3-x} nanorods are shown in Figs.
168 2D and E, respectively, which can be deconvoluted into two peaks. The peak O_1 at 530.7 eV results

from lattice oxygen. The peak O_2 at 532.3 eV is ascribed to surface chemisorbed oxygen. The area ratio of peak O_2 to peak O_1 for MoO_3 nanorods is 0.59, which is lower than that of 0.80 for MoO_{3-x} nanorods, indicating that oxygen vacancies contribute to increasing the surface adsorption of oxygen species [36].

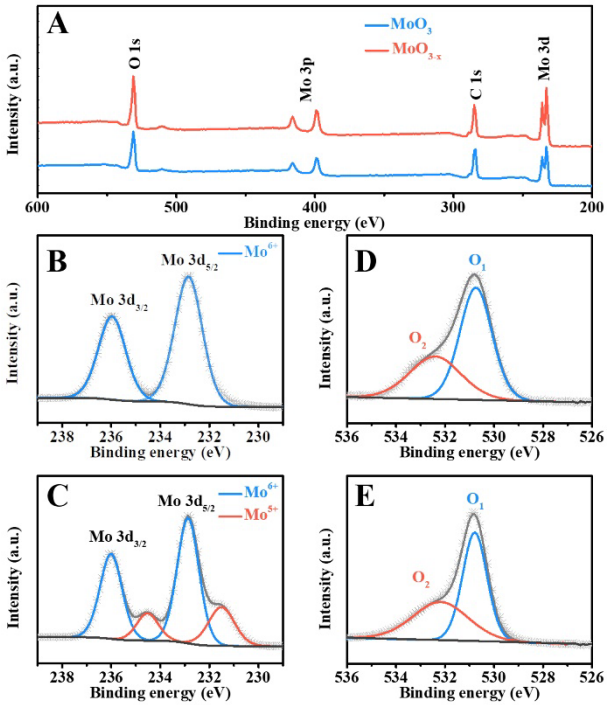

Fig. 2 (A) XPS survey spectra of MoO_3 and MoO_{3-x} nanorods, XPS spectra of (B-C) Mo 3d and (D-E) O 1s for MoO_3 nanorods and MoO_{3-x} nanorods, respectively.

The morphology and microstructure of the MoO_{3-x} were identified by SEM and TEM. In Fig. 3A, the MoO_3 presents uniform and rod-like nanostructure with smooth surface. As shown in Fig. 3B, the morphology of MoO_{3-x} is the same that of the MoO_3, which indicates that the introduction of oxygen vacancies does not affect the morphology. The length and width of MoO_{3-x} nanorods were confirmed by TEM images (Figs. 3C and D). It can be seen that the length is ~ 9 μm (Fig. 3C) and the width is ~ 200 nm (Fig. 3D). In Fig. 3E, the well-defined lattice fringes are observed for MoO_{3-x} nanorods. The interplanar distances are 2.332 and 2.702 Å, which are attributed to the (131) and (101) crystal planes of the α-MoO_3 (JCPDS No. 05–0508), respectively [26]. Additionally, there are some disorder and

discontinuous lattice fringes, as seen in the ellipse marks in Fig. 3E, which further proves the introduction of oxygen vacancies in MoO_{3-x} nanorods. In Fig. 3F, a single crystal nature is observed for MoO_{3-x} nanorods by selected area electron diffraction (SAED) pattern. Equally, the exposed crystal planes of (200), (202), and (002) could be well indexed to orthorhombic phase α-MoO_3, which coincides well with the XRD results [26,28]. The unique morphology and element composition of MoO_{3-x} nanorods are further revealed by HAADF-STEM image (Fig. 3G) and EDS elemental mapping (Figs. 3H and I). It clearly demonstrates that these elements of Mo and O are uniformly distributed on the MoO_{3-x} nanorods. Note that atomic ratios of Mo and O (1:2.97) is different with the XPS results (1:2.84). This could result from the XPS is only surface sensitive.

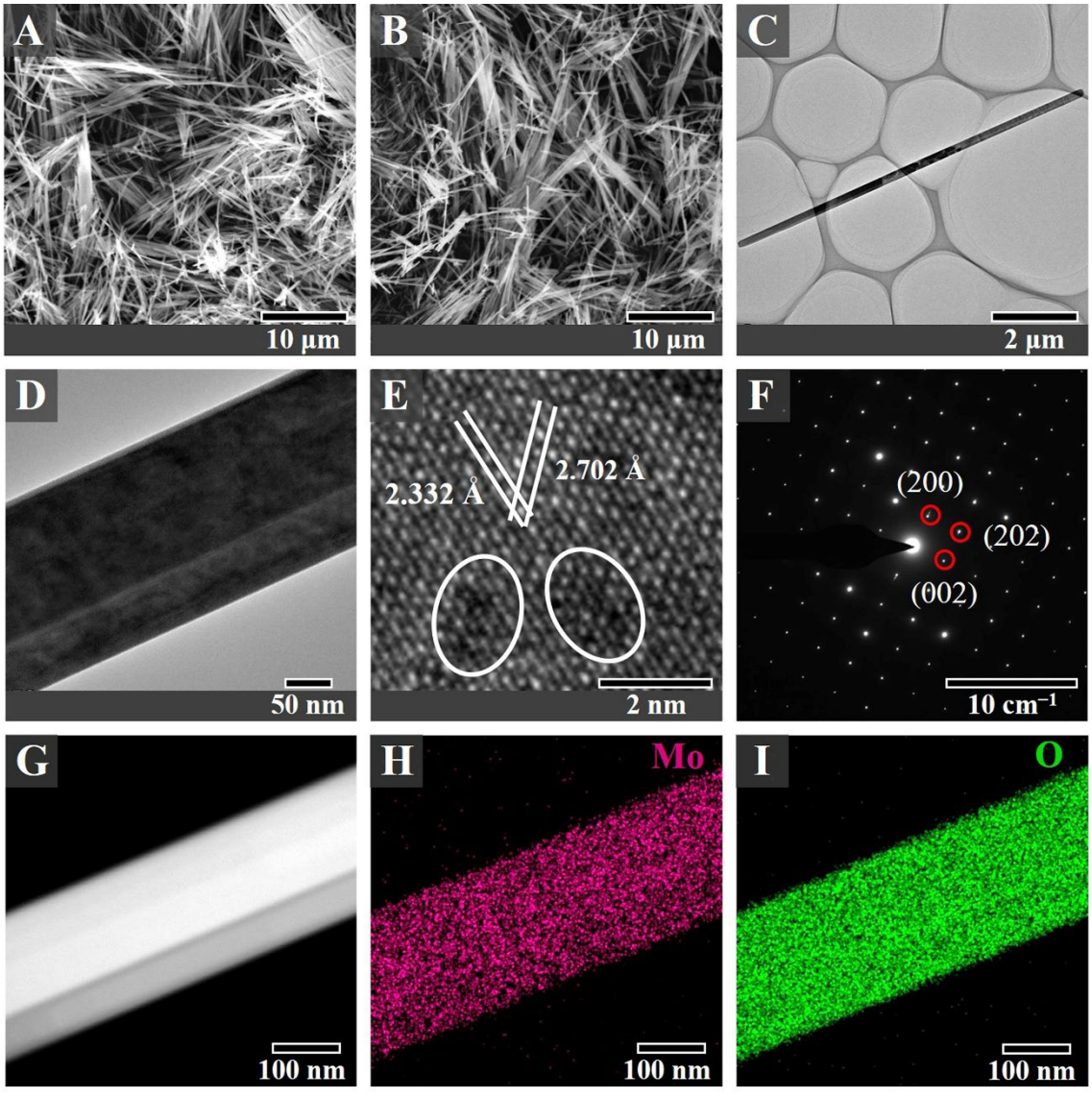

Fig. 3 SEM image of (A) MoO_3 nanorods and (B) MoO_{3-x} nanorods. (C-D) TEM image, (E) HRTEM image, (F) SAED patterns, (G) HAADF-STEM image, and (H-I) corresponding EDS elemental mapping images of MoO_{3-x} nanorods.

To further verify the presence of oxygen vacancies in MoO_{3-x} nanorods, the ESR spectra of as-prepared MoO_3 and MoO_{3-x} nanorods were recorded, as shown in Fig. 4A. It can be seen that there is no visible ESR signal for pristine MoO_3 nanorods. In sharp contrast, an intense signal at g = 2.003 is observed for MoO_{3-x} nanorods. The results suggest that the oxygen vacancies are successfully introduced into MoO_{3-x} nanorods [27,28]. The UV-vis diffuse reflectance spectra of as-prepared MoO_3 and MoO_{3-x} nanorods were collected to evaluate the optical absorption capacity of photocatalyst. In Fig. 4B, the absorption edge of the pristine MoO_3 nanorods is about 400 nm. Besides, no significant absorption is observed in the visible region. In contrast, the MoO_{3-x} nanorods display the strong absorption in the visible region, which results from the existence of oxygen vacancies [27]. The band gap (E_g) of MoO_{3-x} nanorods is 3.24 eV, which is lower than that of pristine MoO_3 nanorods (3.29 eV) (Fig. 4C), indicating that oxygen vacancies could improve the photocatalytic activity [37]. The recombination feature of photogenerated carriers in MoO_3 and MoO_{3-x} nanorods was studied by using PL spectra. As shown in Fig. 4D, there is a clear emission band at ~ 688 nm for both samples [38,39]. Note that the peak of MoO_3 nanorods exhibits a higher intensity than that of MoO_{3-x} nanorods, revealing that the recombination rate of photoexcited electrons and holes is cut down after introduction of oxygen vacancies. The Mott-Schottky plot of MoO_{3-x} nanorods displays a positive slope (Fig. 4E), suggesting that MoO_{3-x} nanorods is a n-type semiconductor [40]. The flat band potential (V_{fb}) of MoO_{3-x} nanorod is determined to be 2.75 V (vs. Li^+/Li), closing to CB for n-type semiconductor [41]. According to the formula: $E_{VB} = E_{CB} + E_g$, the potentials of CB (E_{CB}) and VB (E_{VB}) for MoO_{3-x} nanorod are calculated to be 2.75 V and 5.99 V (vs. Li+/Li), respectively, which spans the equilibrium potential of battery reaction (2.96 V *vs.* Li^+/Li) [42]. Additionally, the potentials of CB (E_{CB}) and VB (E_{VB}) of

MoO_{3-x} nanorods cab be calculated by the empirical equation [43]: $E_{VB}= X-E_e + 0.5E_g$, where X is the absolute electronegativity of MoO_{3-x} nanorods (6.40 eV) [44]; E_e is the energy of free electrons of the hydrogen scale (4.5 eV) [45]. According to the above equation, E_{VB} and E_{CB} of MoO_{3-x} nanorods are calculated to be 2.76 V and 5.98 V (vs. Li^+/Li) respectively, which are in accordance with the results calculated by Mott-Schottky. Thereby, the MoO_{3-x} nanorods will contribute to accelerating the ORR and OER processes under illumination, which is illustrated in Fig. 4F. During discharge, the photoelectrons excited in the CB will boost the formation of Li_2O_2. Meantime, the holes are leaved in VB and reduced via the electrons in an external circuit. During charge, the holes in VB can facilitate the decomposition of Li_2O_2 and photoelectrons reduce Li^+ at anode by the external circuit. Thus, MoO_{3-x} nanorods are considered as the promising photocatalysts for photo-assisted Li-O_2 batteries.

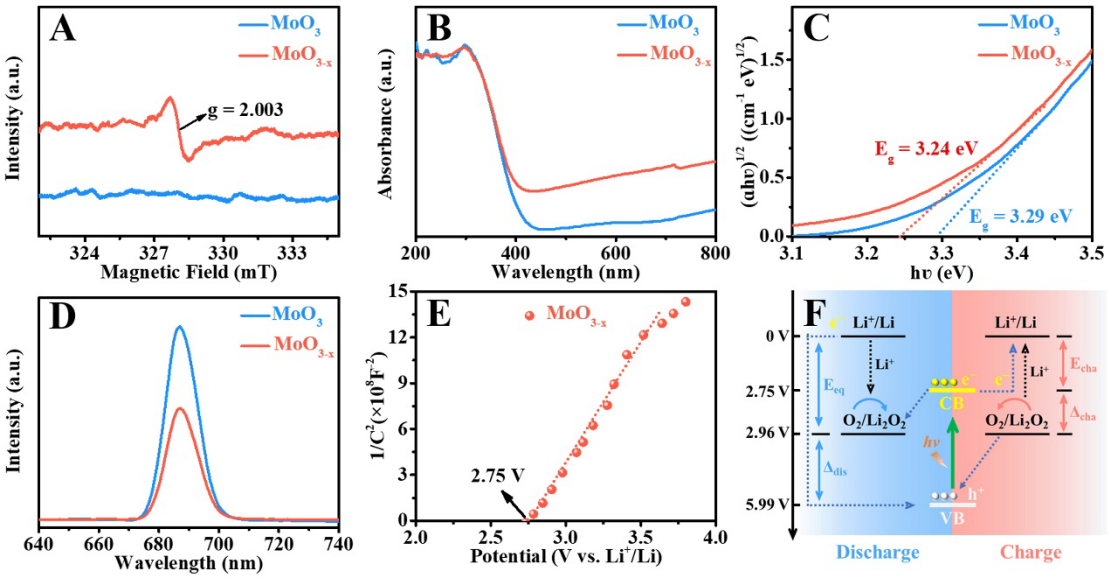

Fig. 4 (A) ESR spectra, (B) UV-vis spectra, (C) the corresponding Kubelke-Munk transformed spectra, and (D) PL spectra of MoO_3 and MoO_{3-x} nanorods. (E) Mott-Schottky plot of MoO_{3-x} nanorods. (F) Schematic energy diagram of a Li-O_2 cell using MoO_{3-x} nanorods as catalyst with illumination.

To identify the effect of oxygen vacancies on electrochemical process of photo-assisted Li-O_2 batteries, CV curves of the cells using MoO_3 and MoO_{3-x} nanorods as catalyst with/without illumination were recorded in an O_2 atmosphere. As shown in Fig. 5A, the cell with MoO_{3-x} nanorods

under light shows a higher onset potential and larger anodic current in ORR process as well as a lower onset potential and larger cathodic current in OER process than those of the cell with MoO_{3-x} nanorods in dark and the cell with MoO_3 nanorods under light, indicating the high ORR and OER activity of MoO_{3-x} nanorods under illumination [46,47]. Fig. 5B shows the first galvanostatic discharge profiles of Li-O_2 cells based on MoO_3 and MoO_{3-x} catalyst with/without illumination at 200 mA g^{-1} with a cutoff potential of 2.2 V. The discharge capacity of the cell with MoO_{3-x} under light (4035 mAh g^{-1}) is higher than those of the cell with MoO_{3-x} in dark (2390 mAh g^{-1}) and the cell with MoO_3 under light (3342 mAh g^{-1}). Fig. 5C depicts the first discharge and recharge curves of the cells with MoO_3 and MoO_{3-x} nanorods at 100 mA g^{-1} with/without illumination. It can be seen that the discharge and charge potentials are 2.71 and 3.63 V for the cell with MoO_{3-x} in dark, respectively, corresponding to the round-trip efficiency of 74.66%. For the cell with MoO_3 under light, the discharge and charge potentials are 2.78 and 3.58 V and corresponding round-trip efficiency is 77.65%. For the cell with MoO_{3-x} under light, an increased discharge potential of 2.86 V and a reduced charge potential of 3.08 V are obtained, which shows an ultrahigh round-trip efficiency of 92.86%. The rate performance of the Li-O_2 cells with MoO_3 and MoO_{3-x} at various current densities of 100, 200, and 500 mA g^{-1} is evaluated with/without illumination (Figs. 5D-F). In Fig. 5D, the overpotentials for the cell with MoO_{3-x} under light are 0.22, 0.48, and 0.87 V at 100, 250 and 500 mA g^{-1}, corresponding to the round-trip efficiency of 92.86%, 85.32%, and75.69%, respectively. The slightly increased overpotential and reduced round-trip efficiency could be caused by the restricted photogenerated electrons contributing to the compensative current [15]. Note the overpotentials for cells with MoO_{3-x} under light are still lower than those of the cells with MoO_{3-x} in dark (Fig. 5E) and the cells with MoO_3 under light (Fig. 5F). Additionally, the cyclabilities of Li-O_2 cell with MoO_3 and MoO_{3-x} catalyst were investigated at 250 mA g^{-1} under 500 mAh g^{-1} with/without illumination. The cycle life of the cell with MoO_{3-x} reaches 100 cycles under light (Figs. 6A and D). In contrast, the cell with MoO_{3-x} keeps 30 cycles in dark (Figs. 6B and D) and the cell with MoO_3 shows 30 cycles under light (Figs. 6C and D). These

results indicate that MoO_{3-x} nanorods as catalyst is beneficial to facilitate ORR and OER processes in photo-assisted Li-O_2 batteries, demonstrating the advancement of introducing oxygen vacancies into MoO_3.

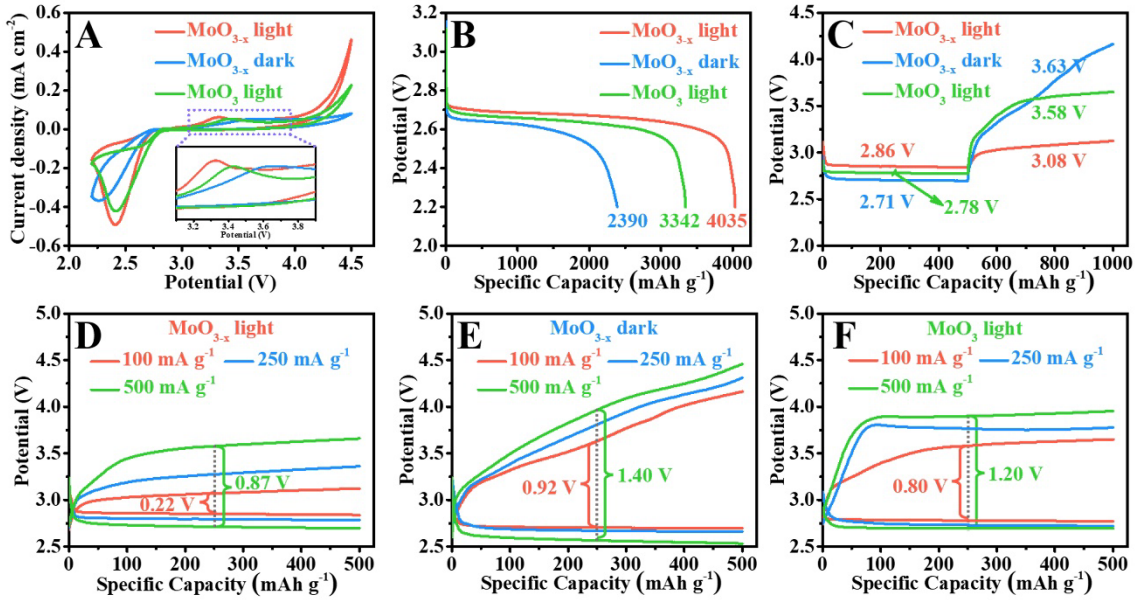

Fig. 5 (A) CV curves of the cells using MoO_3 and MoO_{3-x} nanorods as catalyst with/without illumination; (B) Discharge profiles of the cells using MoO_3 and MoO_{3-x} nanorods as catalyst with/without illumination; (C) the first discharge and recharge curves of the cells with MoO_3 and MoO_{3-x} nanorods at 100 mA g^{-1} with/without illumination; (D-F) the first discharge and charge curves of the Li-O_2 cells with MoO_3 and MoO_{3-x} at various current densities with/without illumination.

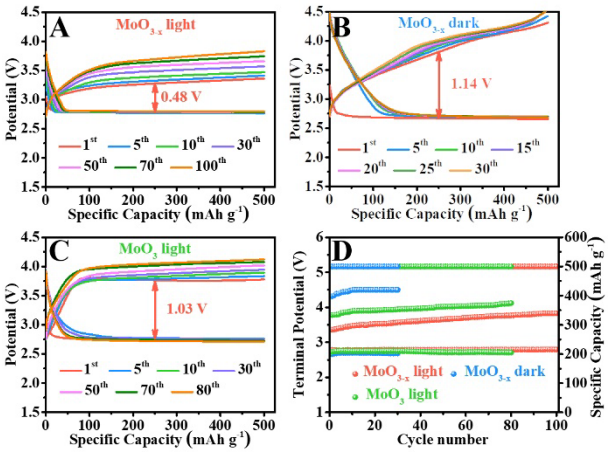

Fig. 6 (A-C) The continuously discharge and charge curves of the cells using MoO_3 and MoO_{3-x} nanorods as catalyst with/without illumination; (D) corresponding the cycle number associated with terminal discharge/charge voltage and delivered discharge.

Fig. 7A shows the LSV curves for the Li-O_2 cells using MoO_3 and MoO_{3-x} nanorods as catalyst at a scan rate of 0.5 mV s^{-1} within a potential range of 2.4-3.0 V with/without illumination. The cell with MoO_{3-x} nanorods under light exhibits an improved onset potential than those of the cell with MoO_{3-x} nanorods in dark and the cell with MoO_3 nanorods under light, which suggests a positive effect of both oxygen vacancies and light assistant on ORR process. Based on the LSV curves, Tafel slope were obtained, as shown in Fig. 7B. The cell with MoO_{3-x} nanorods under light shows a lower Tafel slope value of 117 mV dec^{-1} than those of the cell with MoO_{3-x} nanorods in dark of 194 mV dec^{-1} and the cell with MoO_3 nanorods under light of 129 mV dec^{-1}, proving a fast electron migration rate for ORR process for a cell with MoO_{3-x} nanorods under light. Additionally, to assess the reaction kinetics of MoO_{3-x} nanorods with illumination during OER process, the preloaded Li_2O_2 cells were prepared based on commercial Li_2O_2. The LSV curves for the preloaded Li_2O_2 cells using MoO_3 and MoO_{3-x} nanorods as catalyst at a scan rate of 0.5 mV s^{-1} within a potential range of 3.0-4.5 V with/without illumination are displayed in Fig. 7C. It can be seen that the cell with MoO_{3-x} nanorods under light shows a lower onset potential and larger cathodic current than those of the cell with MoO_{3-x} nanorods in dark and the cell with MoO_3 nanorods under light, indicating a positive effect of both oxygen vacancies and light assistant on OER process. Equally, Tafel slope of the cell with MoO_{3-x} nanorods under light was calculated to be 472 mV dec^{-1}, which is lower than those of the cell with MoO_{3-x} nanorods in dark of 1469 mV dec^{-1} and the cell with MoO_3 nanorods under light of 686 mV dec^{-1}, further demonstrating the rapid electron migration rate for the OER process for a cell with MoO_{3-x} nanorods under light (Fig. 7D). Therefore, the cell with MoO_3 nanorods under light exhibit superior

reaction kinetics during ORR and OER processes, which could be ascribed to the effect of both oxygen vacancies and light assistant.

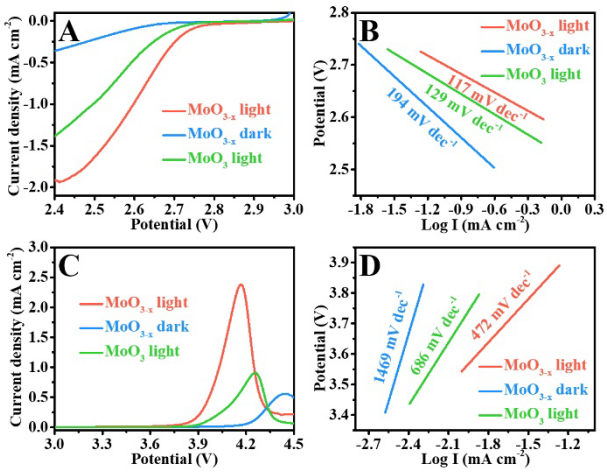

Fig. 7 (A, C) LSV curves of ORR and OER processes for the cells using MoO_3 and MoO_{3-x} nanorods as catalyst with/without illumination and (B, D) corresponding Tafel curves.

The reversibility of the cell with MoO_{3-x} nanorods under illumination was investigated by DEMS to characterize gas consumption and formation during the galvanostatic cycle process. In Fig. 8A, during discharge process, the molar ratio of e^-/O_2 is calculated, which is 2.04, closing to the theoretical value for the O_2 reduction to Li_2O_2. During recharge process, the CO_2 release cannot be detected (Fig. 8A). Equally, the O_2 recovery efficiency is obtained to be 95.3% by calculating the area ration of the O_2 evolution and consumption curves (Figs. 8A and B). These results indicate that the cell with MoO_{3-x} nanorods shows a good reversibility under illumination. In order to identify the discharge products, in-situ XRD is employed to track the cathode for the Li-O_2 cell with MoO_{3-x} under illumination. In Fig. 8C, during the discharge process, the diffraction peaks at 32.9 and 35.0 appear and their intensity gradually increases, which are matched well with Li_2O_2 standard pattern (PDF No. 09-0355), implying that the discharge product is Li_2O_2 [48]. In Fig. 8D, the intensity of Li_2O_2 diffraction peaks gradually reduces until the peaks disappear during subsequent recharge process. Fig. 6E shows the in-situ XRD contour mapping during cycling. Note that the typical diffraction peaks of Li_2O_2 appear during

discharge process and disappear after recharge process, demonstrating that the generation and decomposition of Li_2O_2 is reversible during discharge and charge processes. Additionally, we employed Raman spectrum to characterize the cathodes at the different electrochemical states, as shown in Fig. 8E. After discharge, a peak at 788 cm^{-1} is observed, further indicating that the discharge products are Li_2O_2 [49]. After recharge, the Li_2O_2 peak disappears, suggesting the complete decomposition of formed Li_2O_2, which is consistent with the in-situ XRD results.

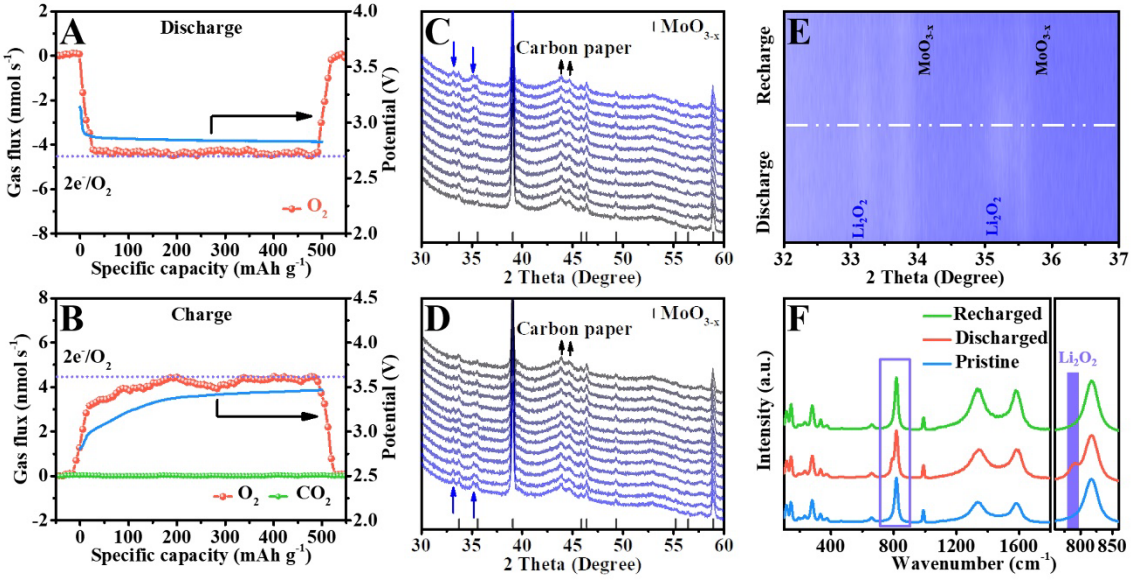

Fig. 8 DEMS results of photo-assisted Li-O_2 batteries with MoO_{3-x} nanorods for the (A) discharge and (B) recharge processes; In-situ XRD patterns of cathode at (C) discharge and (D) recharge processes in photo-assisted Li-O_2 cell with MoO_{3-x} nanorods and (E) corresponding contour mapping; (F) Raman spectra of cathodes at different electrochemical states.

The morphology changes of Li_2O_2 are studied by using SEM to characterize the cathode at 100 mA g^{-1} in different electrochemical states. Compared with the pristine cathode (Fig. S2A in ESM), the SEM image of the discharged cathode shows that the Li_2O_2 is film-like (Fig. 9A). As seen in Fig. 9B, the film-like Li_2O_2 completely removed after recharge. The film-like Li_2O_2 accumulates continuously after deep discharge and their morphology remained unchanged (Fig. S2B in ESM). Note that the reversible formation and decomposition of Li_2O_2 could be maintained up to 50 cycles, as shown in

Figs. 9C and D. Additionally, the morphology of Li_2O_2 was studied at high current densities of 250 and 500 mA g^{-1} was also studied, as shown in Fig. S3 in ESM. It can be seen that the granular-like discharge products form on film-like Li_2O_2 with the increase of current density (Figs. S3A-B in ESM). The granular-like discharge products completely disappear after recharge (Figs. S3C-D in ESM). These results further evidence that Li-O_2 cells with MoO_{3-x} show a superior reversibility under illumination.

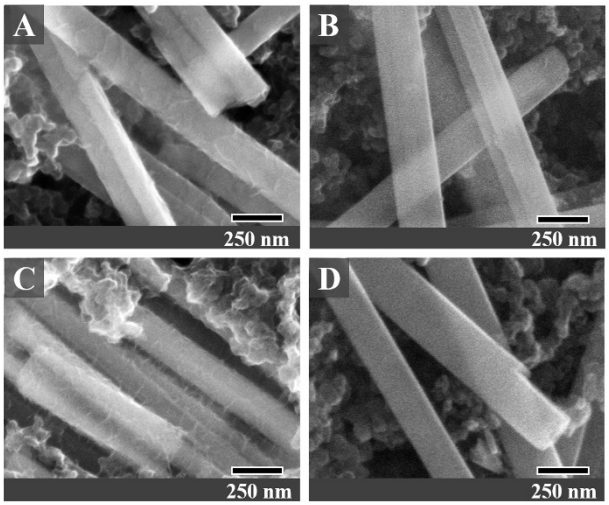

Fig. 9 SEM images of cathode in different electrochemical states of (A) 1st discharged, (B) 1st recharged, (C) 50st discharged, and (D) 50st recharged for photo-assisted Li-O_2 cell with MoO_{3-x} nanorods.

To study the catalytic and photovoltaic advantages of MoO_{3-x} nanorods, the EIS of Li-O_2 cells were collected after different cycles with and without illumination, as shown in Figs. 10A and B, respectively. The Nyquist plots present a semicircle and a diffusive part, which is the classical shape. The insets in Figs. 10A and B show the corresponding equivalent circuit, where R_0 represents the ohmic resistance and R_{ct} corresponds to the charge transfer resistance [50]. The values of R_0, R_{ct}, and R_{total} ($R_{total} = R_0 + R_{ct}$) are fitted by the equivalent circuit, as recorded in Table S1 in ESM and Figs. 10C and D. The values of R_{ct} and R_{total} increase clearly from 1 to 30 cycles for the cell cycled with MoO_{3-x} in dark. In contrast, the values of R_{ct} and R_{total} increase slowly until 100 cycles for the cell

with MoO_{3-x} cycled in light. These results further indicate that MoO_{3-x} nanorods with high photoelectron-catalytic activity can improve the electrochemical microenvironment of photo-assisted Li-O_2 cells and thus accelerate the reaction kinetics.

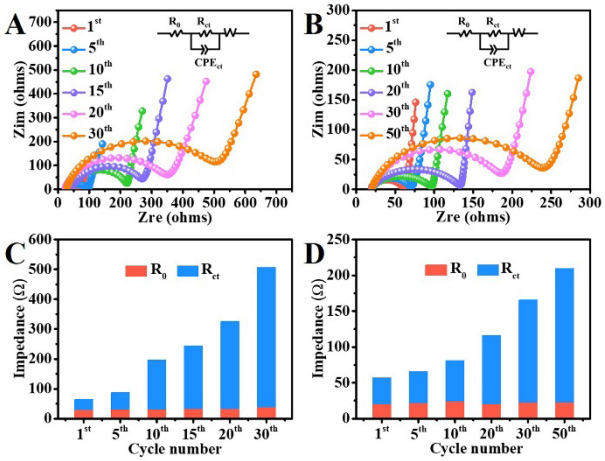

Fig. 10 The Nyquist plots of Li-O_2 cell with MoO_{3-x} nanorods after different cycles (A) without and (B) with illumination and (C-D) the corresponding fitting values of the R_0 and R_{ct}.

4 Conclusions

In summary, the MoO_{3-x} nanorods were successfully synthesized *via* combining solvothermal method and hydrogen-thermal reduction method. In photo-assisted Li-O_2 batteries, the MoO_{3-x} nanorods as photocatalysts not only help to lower the overpotential, but also boost the discharge capacity. In-situ XRD, ex-situ measurements, and electroanalytic techniques indicated that the advanced performances of photo-assisted Li-O_2 batteries could be ascribed to the super photocatalytic ability of MoO_{3-x} nanorods in affording the reversible formation and decomposition of Li_2O_2. The photoexcited electrons and holes on the MoO_{3-x} nanorods are separated effectively under light illumination, which can boost ORR/OER and improve the electrochemical microenvironment. As a result, photo-assisted Li-O_2 batteries with MoO_{3-x} nanorods show an ultralow overpotential of 0.22 V and an ultrahigh round-trip efficiency of 92.86%. We hope that the work can make a contribution to the exploitation of the efficient catalysts for photo-assisted Li-O_2 batteries.

Acknowledgements

This work was supported by the Jilin Province Science and Technology Department Program (Nos. YDZJ202101ZYTS047, YDZJ202201ZYTS304, 20220201130GX, and 20200201187JC), the National Natural Science Foundation of China (Nos. 52171210 and 21978110), the Science and Technology Project of Jilin Provincial Education Department (JJKH20210444KJ and JJKH20220428KJ).

Declaration of competing interest

The authors have no competing interests to declare that are relevant to the content of this article.

Electronic Supplementary Material (ESM)

Electronic Supplementary Material: Supplementary material (The schematic illustration of photo-assisted Li-O_2 battery testing platform; SEM images of cathode at the pristine and different electrochemical states; the fitting values of R_0, R_{ct} and R_{total} of Li-O_2 cell with MoO_{3-x} nanorods after different cycles without and with illumination.) is available in the online version of this article.

References

[1] Huang G, Wang J, Zhang X. Electrode Protection in High-Efficiency Li-O_2 Batteries. *ACS Cent Sci* 2020, **6**: 2136-2148.

[2] Wu C, Yang Q, Zheng Z, *et al.* Boosting Na-O_2 battery performance by regulating the morphology of NaO_2. *Energy Storage Mater* 2023, **54**: 1-9.

[3] Kwak WJ, Rosy, Sharon D, *et al*. Lithium-oxygen batteries and related systems: potential, status, and future. *Chem Rev* 2020, **120**: 6626-6683.

[4] Hu X, Luo G, Zhao Q, *et al.* Ru single atoms on N-doped carbon by spatial confinement and ionic substitution strategies for high-performance Li-O_2 batteries. *J Am Chem Soc* 2020, **142**: 16776-16786.

[5] Liu Y, Hou Y, Liu L, *et al.* Nanostructured Carbon-based Cathode Materials for Non-aqueous Li-O_2 Batteries. *Mater Lab* 2022, **1**: 220015.

[6] Gao R, Zhou D, Ning D, *et al.* Probing the Self-Boosting Catalysis of $LiCoO_2$ in Li-O_2 Battery with Multiple In Situ/Operando Techniques. *Adv Funct Mater* 2020, **30**: 2002223.

[7] Zhao Q, Katyal N, Seymour ID, *et al.* Vanadium (III) acetylacetonate as an efficient soluble catalyst for lithium-oxygen batteries. *Angew Chem Int Ed* 2019, **131**: 12683-12687.

[8] He B, Li G, Li J, *et al*. $MoSe_2$@ CNT core-shell nanostructures as grain promoters featuring a direct Li_2O_2 formation/decomposition catalytic capability in lithium-oxygen batteries. *Adv Energy Mater* 2021, **11**: 2003263.

[9] Liu X, Huang Q, Wang J, *et al*. In-situ deposition of Pd/Pd_4S heterostructure on hollow carbon spheres as efficient electrocatalysts for rechargeable Li-O_2 batteries. *Chinese Chem Lett* 2021, **32**: 2086-2090.

[10] Jeong YS, Park JB, Jung HG, *et al.* Study on the catalytic activity of noble metal nanoparticles on reduced graphene oxide for oxygen evolution reactions in lithium-air batteries. *Nano Lett* 2015, **15**: 4261-4268.

[11] Sun G, Li F, Wu T, *et al*. O_2 adsorption associated with sulfur vacancies on MoS_2 microspheres. *Inorg Chem* 2019, **58**: 2169-2176.

[12] Zhang G, Li G, Wang J, *et al*. 2D SnSe Cathode Catalyst Featuring an Efficient Facet-Dependent Selective Li_2O_2 Growth/Decomposition for Li-Oxygen Batteries. *Adv Energy Mater* 2022, **12**: 2103910.

[13] Lv Q, Zhu Z, Zhao S, *et al.* Semiconducting metal-organic polymer nanosheets for a photoinvolved Li-O_2 battery under visible light. *J Am Chem Soc* 2021, **143**: 1941-1947.

[14] Jiao H, Sun G, Wang Y, *et al.* Defective TiO_2 hollow nanospheres as photo-electrocatalysts for photo-assisted Li-O_2 batteries. *Chinese Chem Lett* 2022, **33**: 4008-4012.

[15] Li M, Wang X, Li F, *et al.* A Bifunctional Photo-Assisted Li-O_2 Battery Based on a Hierarchical Heterostructured Cathode. *Adv Mater* 2020, **32**: 1907098

[16] Li D, Lang X, Guo Y, *et al.* A photo-assisted electrocatalyst coupled with superoxide suppression for high performance Li-O_2 batteries. *Nano Energy* 2021, **85**: 105966.

[17] Zulfiqar S, Liu S, Rahman N, *et al.* Construction of S-scheme MnO_2@CdS heterojunction with core-shell structure as H_2-production photocatalyst. *Rare Met* 2021, **40**: 2381-2391.

[18] Cheng Q, Zhang GK. Enhanced photocatalytic performance of tungsten-based photocatalysts for degradation of volatile organic compounds: a review. *Tungsten* 2020, **2**: 240-250.

[19] Jia C, Zhang F, She L, *et al.* Ultra-large sized siloxene nanosheets as bifunctional photocatalyst for a Li-O_2 battery with superior round-trip efficiency and extra-long durability. *Angew Chem Int Ed* 2021, **133**: 11357-11361.

[20] Xue H, Wang T, Feng Y, *et al.* Efficient separation of photoexcited carriers in a g-C_3N_4-decorated WO_3 nanowire array heterojunction as the cathode of a rechargeable Li-O_2 battery. *Nanoscale* 2020, **12**: 18742-18749.

[21] Hu F, Zhang F, Wang X, *et al.* Ultrabroad band microwave absorption from hierarchical MoO_3/TiO_2/$Mo_2TiC_2T_x$ hybrids via annealing treatment. *J Adv Ceram* 2022, **11**: 1466-1478.

[22] Zhu Y, Yao Y, Luo Z, *et al*. Nanostructured MoO_3 for efficient energy and environmental catalysis. *Molecules* 2019, **25**: 18.

[23] Hu C, Xu M, Zhang J, et al. Recyclable MoO_3 nanobelts for photocatalytic degradation of Rhodamine B by near infrared irradiation. *Int J Chem Kinet* 2019, **51**: 3-13.

[24] Hussain MK, Khalid NR. Surfactant-assisted synthesis of MoO_3 nanorods and its application in photocatalytic degradation of different dyes in aqueous environment. *J Mol Liq* 2022, **346**: 117871.

[25] Sajadi M, Ranjbar M, Rasuli R. Two-step synthesis of Ag-decorated MoO_3 nanotubes, and the effect of hydrogen doping. *Appl Surf Sci* 2020, **527**: 146675.

[26] Zhou Z, Wang Y, Peng F, *et al.* Intercalation-Activated Layered MoO_3 Nanobelts as Biodegradable Nanozymes for Tumor-Specific Photo- Enhanced Catalytic Therapy. *Angew Chem Int Ed* 2022, **134**: e202115939.

[27] Liu Q, Wu Y, Zhang J, *et al.* Plasmonic MoO_{3-x} nanosheets with tunable oxygen vacancies as efficient visible light responsive photocatalyst. *Appl Surf Sci* 2019, **490**: 395-402.

[28] Chen YY, Zhang Y, Zhang X, *et al.* Self-templated fabrication of $MoNi_4/MoO_{3-x}$ nanorod arrays with dual active components for highly efficient hydrogen evolution. *Adv Mater* 2017, **29**: 1703311.

[29] Zhang S, Wang G, Jin J, *et al.* Self-catalyzed decomposition of discharge products on the oxygen vacancy sites of MoO_3 nanosheets for low-overpotential Li-O_2 batteries. *Nano Energy* 2017, **36**: 186-196.

[30] Hanson ED, Lajaunie L, Hao S, *et al.* Systematic study of oxygen vacancy tunable transport properties of few-layer MoO_{3-x} enabled by vapor-based synthesis. *Adv Funct Mater* 2017, **27**: 1605380.

[31] Ji F, Ren X, Zheng X, *et al.* 2D-MoO_3 nanosheets for superior gas sensors. *Nanoscale* 2016, **8**: 8696-8703.

[32] Alsaif MMYA, Latham K, Field MR, *et al.* Tunable plasmon resonances in two-dimensional molybdenum oxide nanoflakes. *Adv Mater* 2014, **26**: 3931-3937.

[33] Ou J Z, Campbell J L, Yao D, *et al.* In situ Raman spectroscopy of H_2 gas interaction with layered MoO_3. *J. Phys Chem C* 2011, **115**: 10757-10763.

[34] Zhang Y, Chen P, Wang Q, *et al.* High-capacity and kinetically accelerated lithium storage in MoO_3 enabled by oxygen vacancies and heterostructure. *Adv Energy Mater* 2021, **11**: 2101712.

[35] Chu K, Luo Y, Shen P, *et al.* Unveiling the Synergy of O-Vacancy and Heterostructure over MoO_{3-x} /MXene for N_2 Electroreduction to NH_3. *Adv Energy Mater* 2022, **12**: 2103022.

[36] Wang F, Dong B, Wang J, *et al.* Self-supported porous heterostructure WC/WO_{3-x} ceramic electrode for hydrogen evolution reaction in acidic and alkaline media. *J Adv Ceram* 2022, **11**: 1208-1221.

[37] Luo Z, Miao R, Huan TD, *et al.* Mesoporous MoO_{3-x} material as an efficient electrocatalyst for hydrogen evolution reactions. *Adv Energy Mater* 2016, **6**: 1600528.

[38] Liu X, Luo Y, Ling C, *et al.* Rare earth La single atoms supported MoO_{3-x} for efficient photocatalytic nitrogen fixation. *Appl Catal B: Environ* 2022, **301**: 120766.

[39] Guan X, Ren Y, Chen S, *et al.* Charge separation and strong adsorption-enhanced MoO_3 visible light photocatalytic performance. *J Mater Sci* 2020, **55**: 5808-5822.

[40] Li Y, Jin Z, Wang H, *et al.* Effect of electron-hole separation in MoO_3@Ni_2P hybrid nanocomposite as highly efficient metal-free photocatalyst for H_2 production. *J Colloid Interf Sci* 2019, **537**: 629-639.

[41] Mohamed MM, Salama TM, Morsy M, *et al.* Facile strategy of synthesizing α-MoO_{3-x} nanorods boosted as traced by 1% graphene oxide: Efficient visible light photocatalysis and gas sensing applications. *Sensor Actuat B: Chem* 2019, **299**: 126960.

[42] Wei L, Su Y, Ma Y, *et al.* Photoluminescent WSe_2 nanofibers as freestanding cathode for Solar-assisted Li-O_2 battery with ultrahigh capacity and transparent casing. *Chem Eng J* 2022, **448**: 137591.

[43] Shang Y, Chen X, Liu W, *et al*. Photocorrosion inhibition and high-efficiency photoactivity of porous g-C_3N_4/Ag_2CrO_4 composites by simple microemulsion-assisted co-precipitation method. *Appl Catal B-Environ* 2017, **204**: 78-88.

[44] Zheng F, Dong F, Lv Z, *et al*. A novel g-C_3N_4/tourmaline composites equipped with plasmonic MoO_{3-x} to boost photocatalytic activity. *Colloid Interf Sci* 2021, **43**: 100434.

494 [45] Huang L, Xu H, Zhang R, *et al*. Synthesis and characterization of g-C_3N_4/MoO_3 photocatalyst
495 with improved visible-light photoactivity. *Appl Surf Sci* 2013, **283**: 25-32.
496 [46] Zhang G, Liu C, Guo L, *et al*. Electronic "Bridge" Construction via Ag Intercalation to Diminish
497 Catalytic Anisotropy for 2D Tin Diselenide Cathode Catalyst in Lithium-Oxygen Batteries. *Adv*
498 *Energy Mater* 2022, **12**: 2200791.
499 [47] Guo L, Tan L, Xu A, *et al*. Highly efficient two-dimensional Ag_2Te cathode catalyst featuring a
500 layer structure derived catalytic anisotropy in lithium-oxygen batteries. *Energy Storage Mater* 2022,
501 **50**: 96-104.
502 [48] Sun G, Gao R, Jiao H, *et al.* Self-formation CoO Nanodots Catalyst in Co(TFSI)$_2$-Modified
503 Electrolyte for High Efficient Li-O$_2$ Batteries. *Adv Mater* 2022, **34**: 2201838.
504 [49] Zhao Q, Wu C, Cong L, *et al.* Yolk-shell Co_2CrO_4 nanospheres as highly active catalysts for Li-
505 O_2 batteries: understanding the electrocatalytic mechanism. *J Mater Chem A* 2017, **5**: 544-553.
506 [50] Liu J, Wu T, Zhang S, *et al.* $InBr_3$ as a self-defensed redox mediator for Li-O_2 batteries: in situ
507 construction of a stable indium-rich composite protective layer on the Li anode. *J Power Sources* 2019,
508 **439**: 227095.